Desalination and Water Treatment
www.deswater.com
doi: 10.5004/dwt.2018.22394

114 (2018) 251–264
May

Visible-light active and magnetically recyclable Ag-coated Fe_3O_4/TiO_2 nanocomposites for efficient photocatalytic oxidation of 2,4-dichlorophenol

Narjes Esmaeili[a], Azadeh Ebrahimian Pirbazari[a,b,*], Ziba Khodaee[c]

[a]*Caspian Faculty of Engineering, College of Engineering, University of Tehran, P.O. Box 43841-119, Rezvanshahr 43861-56387, Iran, email: narjes.esmaeili@ut.ac.ir (N. Esmaeili)*
[b]*Fouman Faculty of Engineering, College of Engineering, University of Tehran, P.O. Box 43515-1155, Fouman 43516-66456, Iran, Tel. +981334734927; Fax: +981334737228; email: aebrahimian@ut.ac.ir*
[c]*University of Applied Science and Technology, P.O. Box 41635-3697, Guilan, Iran, email: zibakhodaee@uast.ac.ir*

Received 16 November 2017; Accepted 21 April 2018

ABSTRACT

Fe_3O_4/TiO_2/Ag nanocomposites with different amounts of silver were prepared using the sol–gel method. X-ray diffraction, energy-dispersive X-ray spectroscopy, field-emission scanning electron microscopy, transmission electron microscopy, diffuse reflectance spectroscopy, Brunauer–Emmett–Teller surface areas, and the vibration sample magnetometry were used to characterize these nanocomposites. Photocatalytic activity of the nanocomposites was examined via decomposing the solution of 2,4-dichlorophenol (2,4-DCP) exposed to UV/Vis irradiation. Exposing the solution to pure TiO_2 and ternary Fe_3O_4/TiO_2/Ag nanocomposite, we obtained 30% and almost 60% degradation of 2,4-DCP after 180 min irradiation, respectively. The excellent photocatalytic activity of Fe_3O_4/TiO_2/Ag samples can be related to the surface plasmon resonance effect of Ag nanoparticles deposited on Fe_3O_4/TiO_2 nanocomposite. The Fe_3O_4/TiO_2/Ag nanocomposites were retrieved from the solution of reaction through a constant magnetic bar, followed by assessing their photocatalytic activity after three repetitive recycling cycles. Afterward, this nanocomposite might be applied as an efficient and reusable photocatalyst.

Keywords: Ag nanoparticles; Plasmonic photocatalysts; Fe_3O_4; Oxidation; 2,4-Dichlorophenol

1. Introduction

Organic pollutants treatment by the processes of nanomaterials-based advanced oxidation in various wastewaters is among the main environmental concerns [1–3]. To handle this issue via effective procedures for different wastewaters, researchers have focused on advanced oxidation processes because of their ability to generate strongly oxidizing radicals to degrade organic pollutants into harmless chemicals such as CO_2 and H_2O. Heterogeneous photocatalysis using titanium dioxide (TiO_2) is an efficient advanced oxidation method for the fast elimination of organic wastes from the effluent [4–8]. However, the photocatalytic effectiveness of TiO_2 nanomaterials cannot satisfy the practical requirements under sunlight irradiation since the great intrinsic band gap (>3.2 eV) of TiO_2 severely restricts utilization of the visible light. Besides, the fast electron–hole recombination in TiO_2 often results in a low quantum yield and poor photocatalytic activity [9,10]. To use ample and green sunlight appropriately, strategies such as metal/non-metal elements doping and coupling with other functional materials have been selected to generate visible-light-driven TiO_2-based photocatalysts through introducing a natural band gap with lower level of energy, suppressing electron–hole recombination rate, and increasing the surface charge carrier transfer rate of TiO_2 [11–18]. The composite of TiO_2 and metal nanomaterials with a work function lower than the conduction band of TiO_2, such as Ag and Au [19,20], has been found to solve the problem and promote the TiO_2

* Corresponding author.

photocatalytic activity in the UV or visible light region [21–27]. In the photocatalysis process, these metal nanomaterials can function superior electron acceptor/transport materials to enhance the photo-induced electrons' migration and inhibit the charge recombination in electron transfer processes. This function is attributed to the electronic interaction between TiO_2 and these nanoparticles that promotes the photocatalytic performance [28–32]. Ag has been used to develop plasmonic photocatalyst because of indicating the presence of surface plasmon resonance (SPR) at the visible light region [33,34]. In addition, SPR may accelerate the isolation of electrons and holes in a semiconductor catalyst under exposure to visible light [35–37]. It has been evidenced that Ag coupled with semiconductor plasmon resonance provides an efficient tool in the visible region [19,38–43]. Additionally, Ag has decent physicochemical features and great electrical conductivity [44]. Ag nanoparticles in semiconductors may generate Schottky connections, preventing electrons and holes recombination [45]. A major disadvantage of the application of TiO_2 in water treatment is the inconvenience to recycle these photocatalysts due to their good dispersive properties [46–48]. Common isolation techniques, including filtration and centrifugation, can result in catalyst loss and consumption of energy; magnetic separation renders a feasible method for eliminating and recycling materials using external magnetic fields [49–54]. As a typical magnetic material, Fe_3O_4 can solve the problem of TiO_2 photocatalyst recovery when combined with TiO_2. The magnetic TiO_2/Fe_3O_4 composites showed a rapid aggregation under the external magnetic field, which can be useful for separation of these particles in application [55–57].

In the present study, we report the synthesis of TiO_2/Fe_3O_4 nanocomposites containing different quantities of silver (FTA samples). Morphological and structural features of the obtained samples were investigated by different analysis techniques including X-ray diffraction (XRD), field-emission scanning electron microscopy (FESEM)/energy-dispersive X-ray spectroscopy (EDX), diffuse reflectance spectroscopy (DRS), N_2 physisorption, vibration sample magnetometry (VSM), and transmission electron microscopy (TEM) techniques. By employing the photocatalytic oxidation of 2,4-dichlorophenol (2,4-DCP) as a model reaction, we investigated the efficiency of nanocomposites' photoactivity. Chlorophenols are toxic chemicals used in many industrial applications such as petrochemicals, pesticides, dye intermediates, and paints [58]. Especially, 2,4-DCP is an important chemical precursor for the manufacture of a widely used herbicide, 2,4-dichlorophenoxy acetic acid [59]. However, 2,4-DCP may cause some pathological symptoms and changes in human endocrine systems. These compounds are exposed to the skin and gastrointestinal tract. Chlorophenols persistence and bioaccumulation both in animals and in humans has been recently the subject of intense research [60–62]. So, it would be crucial to seek innovative and effective ways to minimize the harm of chlorophenols in the environment. The outstanding properties associated to the prepared nanocomposites suggests that they can be applied as a novel, visible-light harvesting catalyst for given applications in photocatalysis. The ternary nanocomposites exhibited an improved efficiency for 2,4-DCP photocatalytic oxidation.

2. Experimental methodology

2.1. Materials

$FeCl_3 \cdot 6H_2O$ (Merck no. 103943) and $FeSO_4 \cdot 7H_2O$ (Merck no. 103965) were used for the synthesis of Fe_3O_4 nanoparticles (NPs). Tetraisopropyl orthotitanate (TIP, Merck no. 8.21895), anhydrous ethanol, ammonia, and high-purity 2,4-DCP (98%, Merck no. 803774) for photocatalytic experiments as probe molecules were purchased from Merck Company, Germany. Silver nitrate ($AgNO_3$, 99.9%) was obtained from Merck Company, Germany (Merck no. 101510). All the reagents were of analytic grade and applied without additional purification. All aqueous solutions were prepared using double distilled water.

2.2. Preparation of Fe_3O_4 NPs

Fe_3O_4 nanoparticles were synthesized by chemical precipitation technique according to the procedure mentioned by Laurent et al. [63]. In this procedure, the Fe_3O_4 was precipitated under an inert atmosphere (nitrogen 99.999%) and alkaline conditions.

2.3. Preparation of Fe_3O_4/TiO_2 nanocomposite

In this section, 0.1 g Fe_3O_4 NPs was prepared according to the procedure mentioned in section 2.2. Next, 4 mL TIP was mixed with 70 mL anhydrous ethanol and ultrasonicated (ELMA-Germany, E60H, ultrasound bath) for 1 h to form the solution A. Solution B was prepared by diluting 3 mL acetic acid to 90 mL deionized water. Solution B was added to solution A dropwise at 50°C through the mechanical stirring. Then, the solution was stirred for 30 min. Finally, after cooling to room temperature, the solid product from the suspension was separated by employing a magnet, washed with ethanol and water for several times, and dried in a vacuum for 12 h at 60°C. The resultant powder was annealed at 300°C for 1 h to produce an Fe_3O_4/TiO_2 (FT) nanocomposite. From now on, these samples will be shown as FT. Also, pure TiO_2 in the same route was synthesized to control the experiments.

2.4. Ag loading onto TiO_2/Fe_3O_4 sample

The prepared FT sample (section 2.3) was decorated with Ag nanoparticles according to the procedure reported by Huerta Aguilar et al. [64]. For this purpose, 0.5 g of FT was suspended by sonication in 10 mL of deionized water to which $AgNO_3$ (0.5, 1.0, and 2.0 mL, 100.0 mM) was added slowly; the resultant solution was stirred at 20°C for 30 min, and then Na_2CO_3 (0.5 mL, 1.0% w/v) was slowly added. The obtained slurry was separated and dried at room temperature. These nanocomposites were labeled as FTA (a), where (a) is the quantity of silver achieved by EDX analysis.

2.5. Characterization

Using an X-ray detractor (Siemens, D5000, Germany), the XRD patterns were recorded using Cu K_α radiation as the X-ray source. The diffractograms were recorded within the 2θ range of 20°–80°. The morphology of the obtained samples was studied using scanning electron microscope (SEM,

Vegall-Tescan Company, Czech Republic) having an EDX. The UV/Vis diffuse reflectance (DR) spectra of the samples were recorded using an Ava Spec-2048TEC spectrometer. The microstructure and morphology of the prepared samples were studied using a TEM device (Philips CM30 300kV). The nitrogen physisorption assessments were done by a Quantachrome Autosorb-1-MP (Micromeritics). The Brunauer–Emmett–Teller (BET) areas were determined by static nitrogen physisorption at –196°C followed by outgassing at 200°C until the pressure was lower than 5 mbar. VSM was manufactured by Meghnatis Daghigh Kavir Company of Kashan, Iran.

2.6. Photocatalytic oxidation of 2,4-DCP

We selected 2,4-DCP as a model of organic pollutant to study the photocatalytic efficiency of the obtained samples. For photocatalytic oxidation experiments, we used a 500 W OSRAM Halogen lamp (ECO) with a wavelength range of 350–800 nm, and the predominant peak at 575 nm. In each photocatalytic oxidation experiment, the baker containing photocatalyst and 100 mL 2,4-DCP aqueous solution (40 mg/L) in the dark was stirred first for 10 min for desorption/adsorption equilibrium, followed by turning the lamp for 180 min. At certain times, 2 mL of solution were withdrawn and filtered to eliminate the photocatalyst and analyzed using Rayleigh UV-2601 UV/Vis spectrophotometer (λ_{max} = 227 nm).

3. Results and discussion

3.1. X-ray diffraction analysis

Figs. 1 and 2 show the XRD patterns of the synthesized samples. In XRD pattern of Fe_3O_4 NPs (Fig. 1(a)), we detected the characteristic diffractions at 2θ = 30.2°, 35.6°, 43.5°, 54.3°, 57.4°, and 63.1° that are indexed to the reflection of cubic spinel structure of the Fe_3O_4. This result is consistent with those reported using JCPDS card number 19-0629 [65], suggesting that phase purity of Fe_3O_4 and well-resolved diffraction peaks show the good crystallinity of Fe_3O_4 NPs. In XRD pattern of pure TiO_2 (Fig. 1(b)), the strong diffractions at 2θ = 25.3°, 37.7°, 48.0°, 53.8°, 55.0°, and 62.6° confirmed pure anatase phase formation [66]. In XRD pattern of FT sample (Fig. 1(c)), the diffractions became relatively weaker than those of the pure TiO_2 and Fe_3O_4 (Fig. 1(b)) but matched well with the XRD patterns of TiO_2. Also, we detected some weak diffractions of Fe_3O_4 nanoparticles in Fig. 1(b), which may indicate that Fe_3O_4 is coated by TiO_2 and confirm that the sample contains Fe_3O_4 and TiO_2. Figs. 2(a)–(c) showed the XRD patterns of FTA samples. Four peaks at 2θ values of 38.048°, 44.133°, 64.303°, and 77.326° corresponding, respectively, to (111), (200), (220), and (311) planes of silver in the standard powder diffraction card of JCPDS file no. 04-0783 were reported. Due to the low amount, high distribution, and small crystalline dimensions of Ag particles, we did not detect the main diffractions of metallic Ag in XRD pattern of the ternary FTA nanocomposites [67]. Fig. 2(d) shows the XRD pattern of TiO_2/Ag (TA) sample. We detected the main diffractions for anatase phase of TiO_2 in this sample but did not detect the main diffractions for metallic silver.

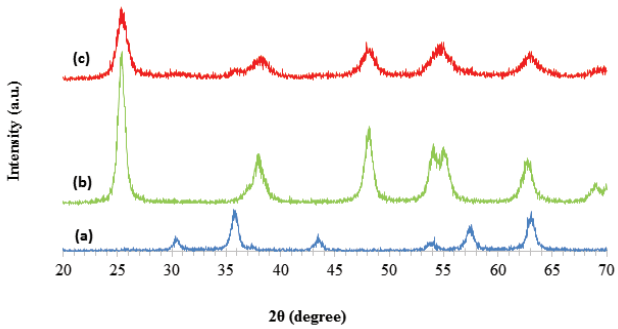

Fig. 1. The XRD patterns of (a) Fe_3O_4, (b) TiO_2, and (c) FT.

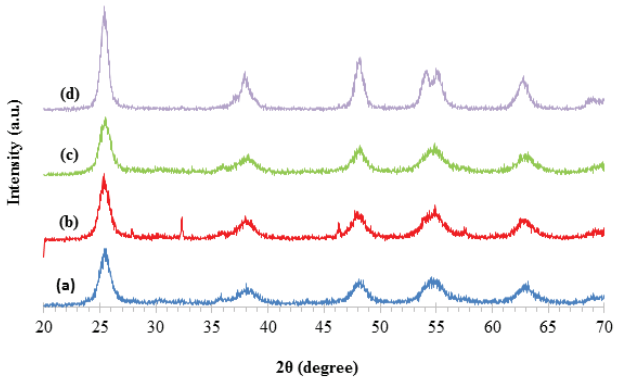

Fig. 2. The XRD patterns of (a) FTA (0.55), (b) FTA (2.09), (c) FTA (3.56), and (d) TA.

The mean TiO_2 crystal size at 2θ = 25.3° using Scherrer equation for each sample was calculated as follows [68]:

$$D = K\lambda/\beta \cos\theta \quad (1)$$

where D is the mean crystallite size; λ is the X-ray wavelength (1.54056 Å); β is the diffraction full width at half maximum in radian; K is a coefficient (0.89); and θ is the angle's diffraction at the peak. The TiO_2 crystal size in all the obtained nanocomposites is within the nanosized range (Table 1).

The lattice parameters ($a = b \neq c$) corresponding to tetragonal crystalline structure were obtained for (101) crystal plane of anatase phase using Eq. (2):

$$1/d^2 = (h^2 + k^2)/a^2 + l^2/c^2 \quad (2)$$

Considering the interplanar spacing (d_{hkl}), the distance between adjacent planes in the set (hkl) can be determined using the Bragg law:

$$d_{hkl} = \lambda/2 \sin\theta \quad (3)$$

The cell volume (tetragonal one) was calculated as:

$$V = a^2c \quad (4)$$

Table 1
Phase, crystal size, and lattice parameters of the prepared samples

Sample	Phase	Crystal size (nm)	$A = b$ (Å)	c (Å)	Cell volume (Å^3)
T	Anatase	10.38	3.77	9.59	136.30
FT	Anatase	7.11	3.79	9.37	134.87
TA	Anatase	8.14	3.77	9.76	138.71
FTA (0.55)	Anatase	8.14	3.78	8.99	127.73
FTA (2.09)	Anatase	8.31	3.80	9.28	134.40
FTA (3.56)	Anatase	7.35	3.78	9.14	130.56

where a and c are considered lattice parameters. Table 1 shows the lattice parameters of prepared samples.

The obtained values of the lattice parameters for TiO_2 in the prepared samples matched well with the TiO_2's anatase structure (JCPDS, 78-2486). The diffraction peaks and lattice parameters of TiO_2 remain unchanged, confirming that silver atoms does not enter the TiO_2 framework and loading on the TiO_2 nanoparticles surface and did not change the crystal structure of TiO_2.

3.2. UV/Vis absorption spectra

The solid-state UV/Vis spectra (Fig. 3(A)) were recorded for all samples. There is a broad intense absorption around 400 nm in the DR spectrum of pure TiO_2, owing to the charge-transfer from the valence band made by 2p orbital's of the oxide anions to the conduction band generated by 3d t_{2g} orbitals of the Ti^{4+} cations [69]. In the DR spectra of FTA samples, we can observe the absorption shoulder peak in the range between 360 and 500 nm. These absorption shoulders result from the post-broadening SPR peak [70]. In the visible region, the existence of localized surface plasmon resonance (LSPR) would enable the ternary nanocomposites to show broad and strong absorption [71,72]. The mechanism concerning the interaction of noble metals mechanism with TiO_2 consists of several and simultaneous processes: Ag NPs deposited on TiO_2 exhibit broad Schottky obstacles functioning as traps of the electron that simplify the electron–hole isolation, improve the process of interfacial electron transfer and also electrons injection into the conduction band, and enhance OH radicals formation efficiency. On the other hand, the spectra of absorption showed that transitions at lower energy are probable since clusters of metal attached to TiO_2 surface bring about localized energy levels within the TiO_2 band gap. As a result, the electrons of valence band are excited at wavelengths above 370 nm [73,74]. We also measured the energy of band gap of the synthesized samples from the DR spectra according to Eq. (5) [75]:

$$[F(R)\,h\upsilon]^{0.5} = A\,(h\upsilon - E_{bg}) \quad (5)$$

where A is a constant, $F(R)$ is the function of Kubelka–Munk, and E_{bg} is the band gap. The E_{bg} data of samples are shown in Table 2. The FTA samples band gap decreased slightly compared with TiO_2 (Table 2). Ag nanoparticles loading on the TiO_2 surface affect the TiO_2 optical properties significantly.

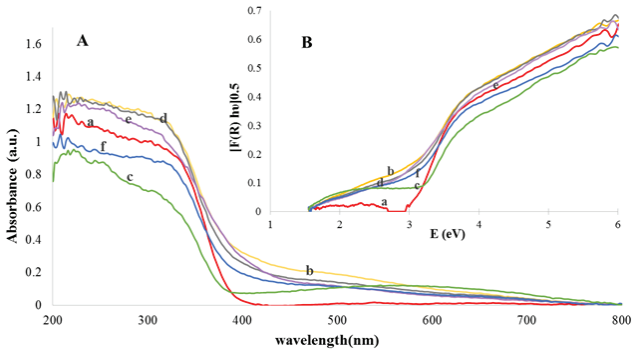

Fig. 3. (A) Diffuse reflectance spectra and (B) Kubelka–Munk plots for the band gap energy calculation of (a) T, (b) FT, (c) TA, (d) FTA (0.55), (e) FTA (2.09), and (f) FTA (3.56).

Table 2
Band gap energy of the prepared samples

Sample	E_{bg} (eV)
T	3.05
FT	2.70
TA	3.02
FTA (0.55)	2.80
FTA (2.09)	2.60
FTA (3.56)	2.85

Evidently, the FTA photoresponse of the nanocomposite is greatly shifted toward the visible light ranges because of the SPR properties of metallic silver nanoparticles. It exhibits a band gap narrowing (2.60 eV) compared with pure TiO_2 (3.05 eV). Fig. 3(B) shows the Kubelka–Munk curves for the synthesized samples.

3.3. FESEM/EDX and TEM analysis

Figs. 4 and 5 show the FESEM images of the synthesized samples at two magnifications. The FESEM images of FTA samples show that TiO_2 coated the Fe_3O_4 surface nanoparticles and exhibit the decoration surface of TiO_2 by metallic silver nanoparticles. To confirm successful decoration of FT nanocomposites with Ag, the samples were analyzed by electron mapping image analysis (Fig. 6). The images of the same particles were obtained for Ti, O, Fe, and Ag. For FTA samples, Ti had a broader distribution compared with Fe, showing that Fe is set in the interior section of the nanocomposites. In comparison, Ti and Ag lie on the outer layer of the nanoparticles of Fe_3O_4. These results indicate that Ag nanoparticles are well spread on the surface of the FT nanocomposite. Fig. 7 displays the EDX spectra analysis of the synthesized samples while Table 3 lists their composition. Among the four elements (Ti, Fe, O, and Ag) presented, the higher Ti content compared with magnetite could be resulting from the formation of the TiO_2 layer coated Fe_3O_4 nanoparticles. The Ag signal is around ~3 keV [76], which may indicate the existence of Ag nanoparticles in photocatalyst. Fig. 8 depicts the TEM image of the best photocatalyst FTA (2.09) at different magnifications. The dark grains of magnetite nanoparticles

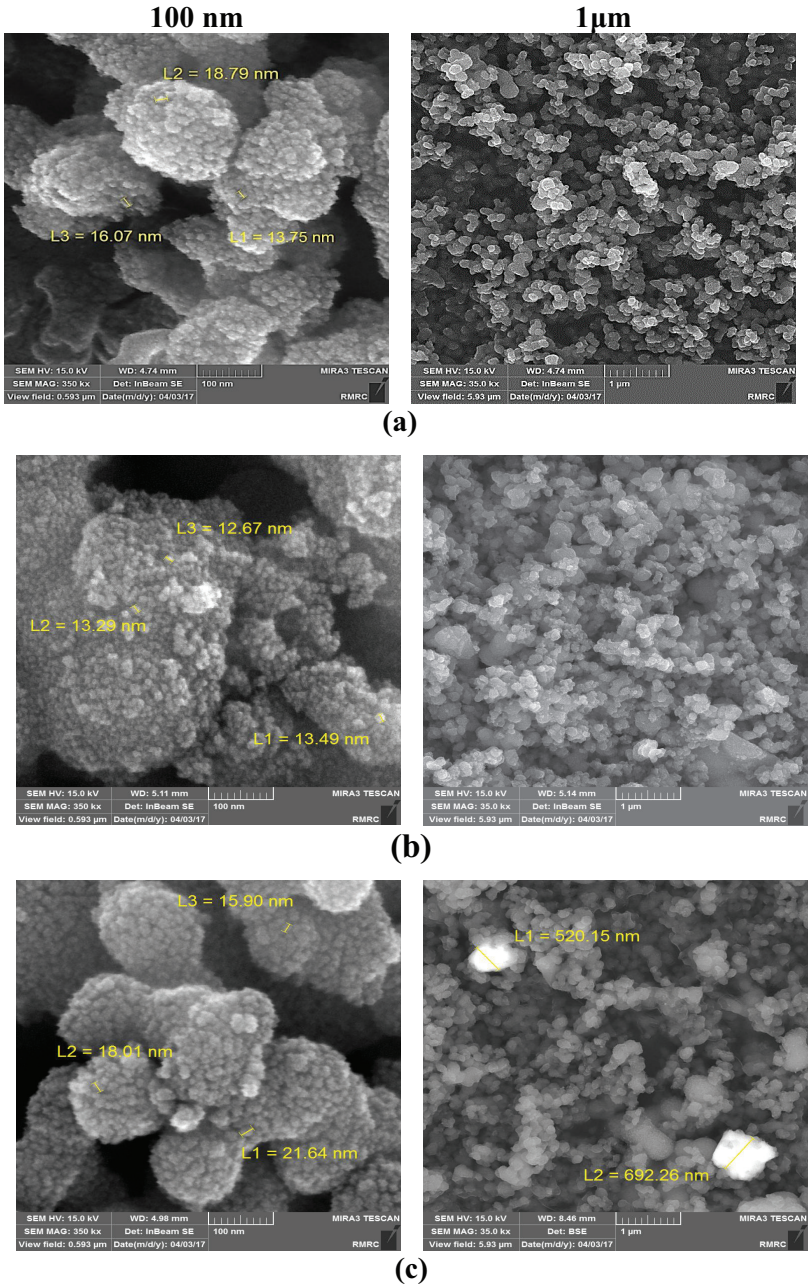

Fig. 4. FESEM images of (a) TiO_2, (b) FT, and (c) TA.

(Fe_3O_4) are fully surrounded via grey TiO_2 layer that contains TiO_2 nanoparticles. Moreover, the TEM images also show that Ag nanoparticles are well dispersed on the FT sample surface.

3.4. N_2 physisorption analysis

The results of N_2 adsorption–desorption isotherms are shown in Fig. 9. The sorption isotherms for the entire prepared samples correspond to the type IV isotherm based on the classification of IUPAC [77]. Textural and structural parameters of the obtained samples are shown in Table 4. Specific surface areas and average pore diameter were calculated according to BET. Pore volumes were extracted from the desorption branch according to the BJH model. The S_{BET} of the FT sample is greater than the pure TiO_2, but the average pore diameter of FT sample is smaller than pure TiO_2. This observation may confirm that the nanolayer of TiO_2 covered the Fe_3O_4 nanoparticles. The BET surface area of the ternary nanocomposites (FTA samples) is greater than that of the starting sample (FT sample), indicating the loading of Ag nanoparticles on the FT sample surface.

3.5. Magnetic properties of the nanocomposites

The saturation magnetization (M_s) of the samples was measured to study the magnetic reaction of the magnetic

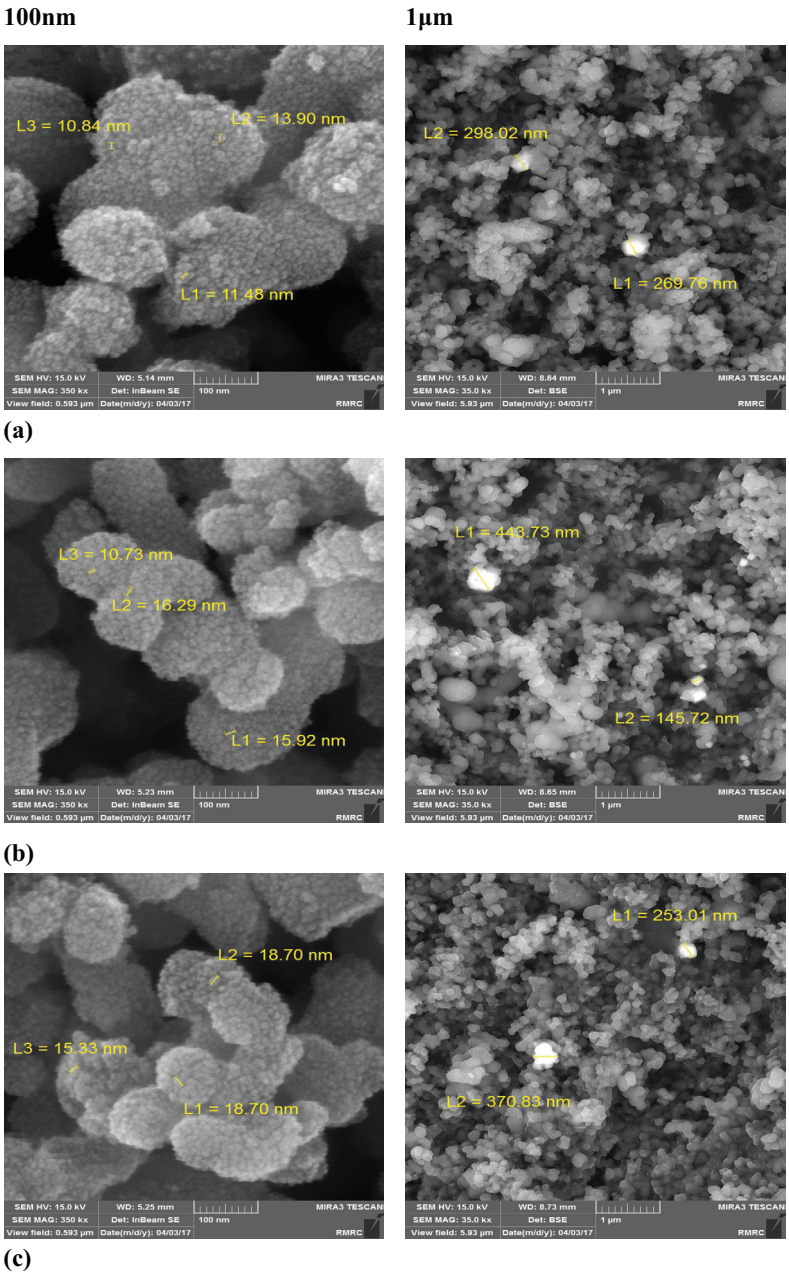

Fig. 5. FESEM images of (a) FTA (0.55), (b) FTA (2.09), and (c) FTA (3.56).

nanocomposites to an external field. According to Fig. 10, the photocatalysts are superparamagnetic at room temperature [78]. It is worth noting that the M_s value of the Fe_3O_4 nanoparticles is significantly higher than that of FT and FTA (a) samples, which is because the Fe_3O_4 nanoparticles are covered with an anatase TiO_2 layer in the FT and FTA (a) samples. The small decrease in M_s value of the FTA (a) samples in comparison with that of the FT sample (Fig. 10) can be explained by the slight increase in mass and size owing to the adherence of Ag nanoparticles to the surface of magnetic composites. Furthermore, no significant variation was seen in the coercivity. Such excellent magnetic properties imply a strong magnetic responsivity on the samples, enabling them to be recycled easily from solution through an external magnetic force. Also, simple, rapid separation and redispersion of the FTA (a) samples can be recognized.

3.6. Photocatalytic oxidation of 2,4-DCP under visible light

To investigate the photocatalytic oxidation activity of the prepared samples for removal of contaminants from wastewater, we selected photocatalytic oxidation of 2,4-DCP as a model reaction. Fig. 11 shows the photocatalytic oxidation of 2,4-DCP under UV/Vis irradiation. Under UV/Vis irradiation, the ternary photocatalyst with 2.09 wt% Ag, FTA (2.09) sample showed the highest performance for 2,4-DCP

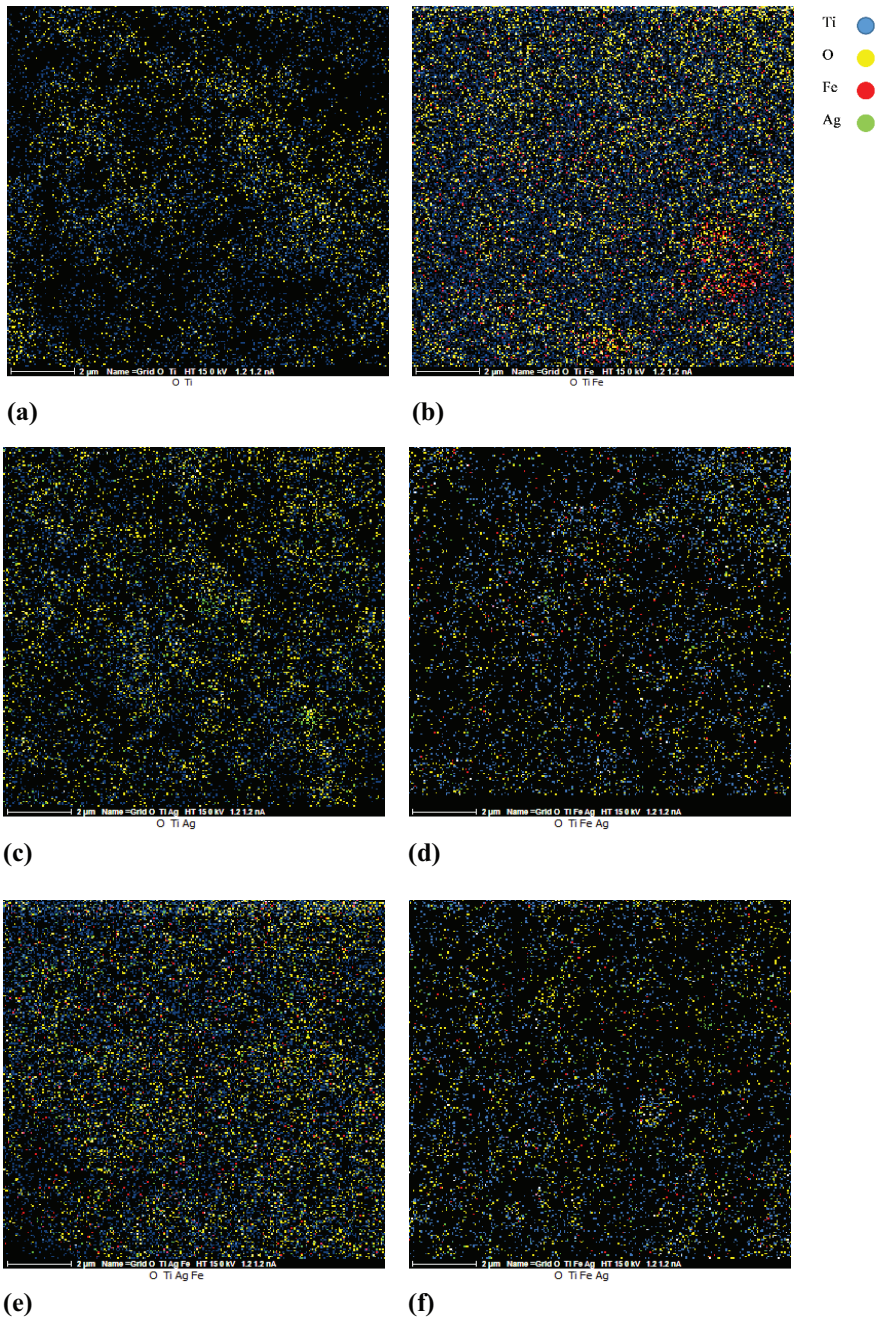

Fig. 6. Elemental mapping of (a) TiO_2, (b) FT, (c) TA, (d) FTA (0.55), (e) FTA (2.09), and (f) FTA (3.56).

photocatalytic oxidation, and we achieved ~55% degradation after 180 min irradiation. The higher photocatalytic efficiency of ternary FTA (a) nanocomposites compared with other photocatalysts can be explained by the SPR influence of Ag nanoparticles and the lower band gap of ternary nanocomposite (Table 2). Fig. 12 shows the mechanism proposed in the present study for the formation of FTA sample and photocatalytic oxidation of 2,4-DCP over FTA sample. In ternary nanocomposites, high-energy electrons were generated because of LSPR of metallic silver nanoparticles under UV/Vis irradiation. These generated electrons were transferred and excited from Ag nanoparticles to the conduction band of TiO_2 and the generated holes remained on the Ag nanoparticles and oxidized the organic target [79]. The adsorbed oxygen molecules on the TiO_2 surface trapped the electron from the conduction band of TiO_2, and thus, some active species such as $OH^{\bullet}$ and $O_2^{\bullet-}$ radicals were produced. These active species attacked 2,4-DCP molecules and decomposed them. Because of the heterojunction formation, many defects exist in TiO_2 that decrease the energy of conduction band of TiO_2 [80] in the ternary nanocomposite. Moreover, TiO_2 can absorb UV/Vis irradiation and generate electrons and holes

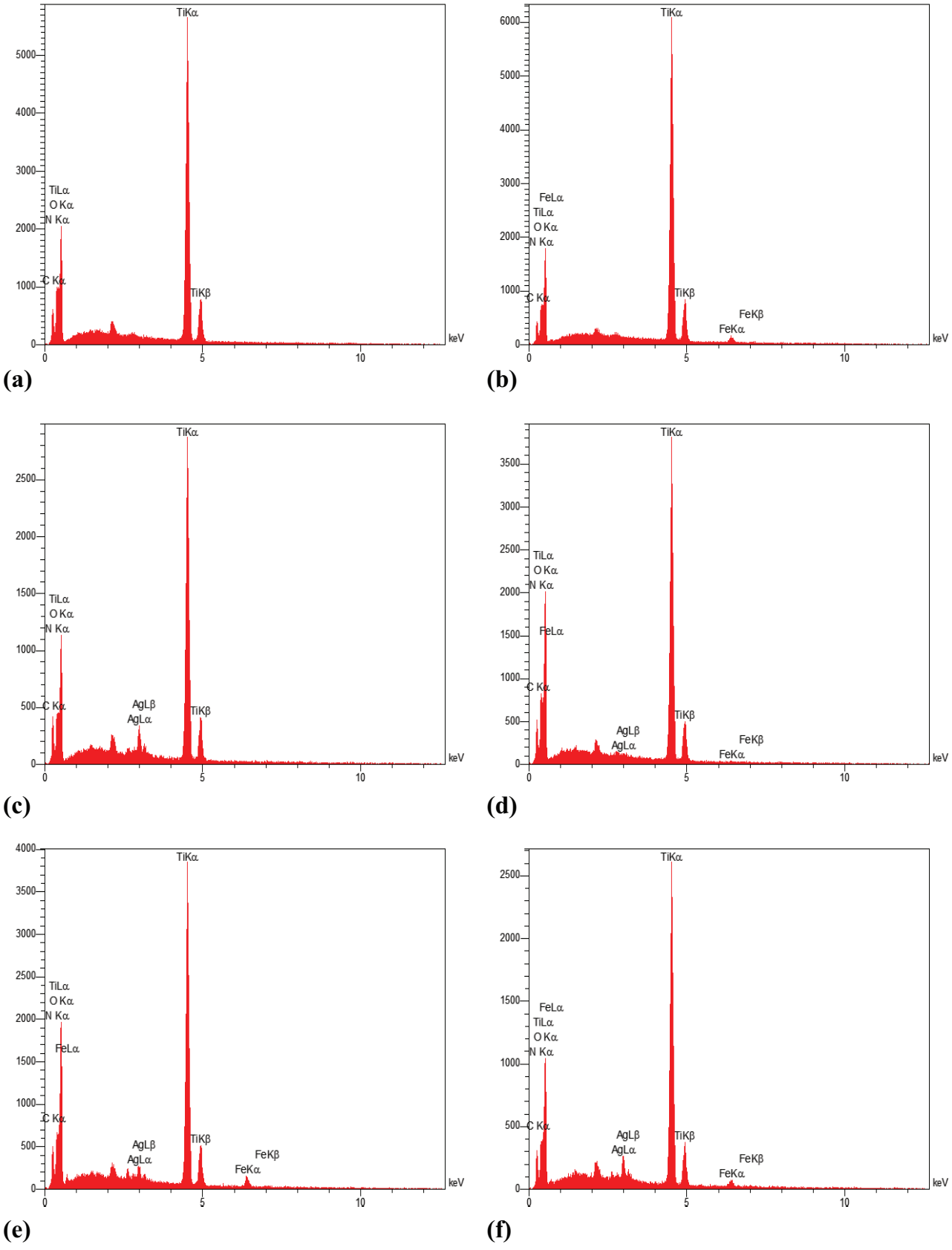

Fig. 7. EDX spectra of (a) TiO_2, (b) FT, (c) TA, (d) FTA (0.55), (e) FTA (2.09), and (f) FTA (3.56).

Table 3
Elemental chemical analysis of the prepared samples

Sample	C (wt%)	N (wt%)	O (wt%)	Ti (wt%)	Fe (wt%)	Ag (wt%)
T	8.12	14.24	41.68	35.96	–	–
FT	6.31	9.80	40.15	41.99	1.75	–
TA	10.26	12.43	37.12	36.13	–	4.06
FTA (0.55)	8.53	15.34	43.82	31.66	0.09	0.55
FTA (2.09)	8.73	12.24	43.84	31.16	1.94	2.09
FTA (3.56)	8.78	11.73	38.60	35.81	1.53	3.56

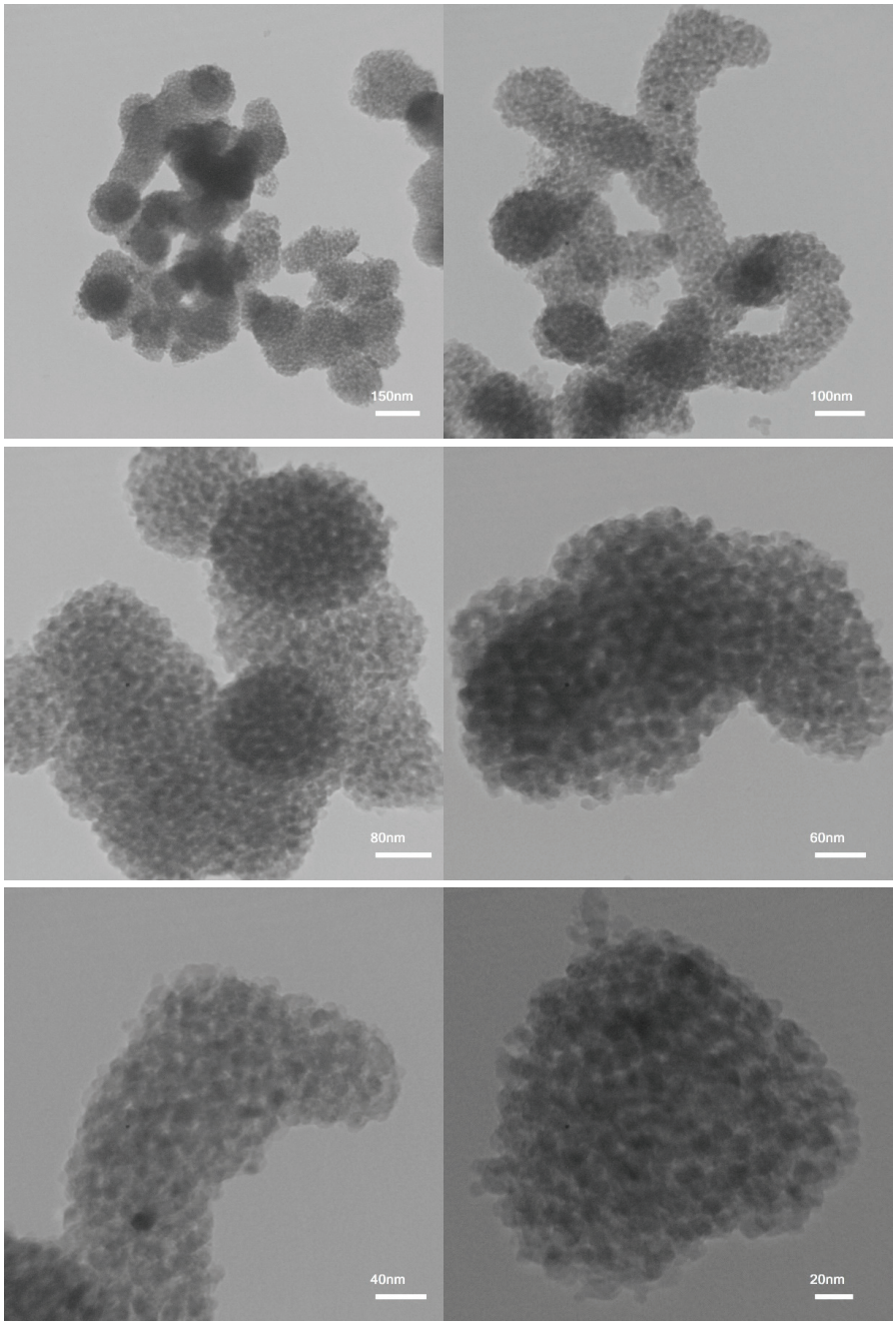

Fig. 8. TEM image of FTA (2.09) nanocomposite at various magnifications.

light. These charge carriers can participate in the destruction of 2,4-DCP and produced more oxygen active species like $OH^{\bullet}$ and $O_2^{\bullet-}$ radicals. Accordingly, the photocatalytic activity was enhanced due to more charge carrier generation. FTA (a) samples can offer a larger surface area (Table 4), contributing to the enhanced photocatalytic function induced by its improved photon absorption [81]. Also, the higher silver loading had shading effect, blocked the light reaching the TiO_2 surface, and resulted in a lower photocatalytic performance [82,83].

3.7. The effect of photocatalyst amount

At low photocatalyst loading, the removal of the organic compound 2,4-DCP increased linearly with the catalyst loading. However, the presence of excess photocatalyst in the aqueous solutions could cause a shielding effect in penetration of light [84]. In this regard, the effect of the photocatalyst dose in suspension was investigated for an optimal condition (Fig. 13). The optimal photocatalyst amount is 10 mg/100 mL for 2,4-DCP degradation.

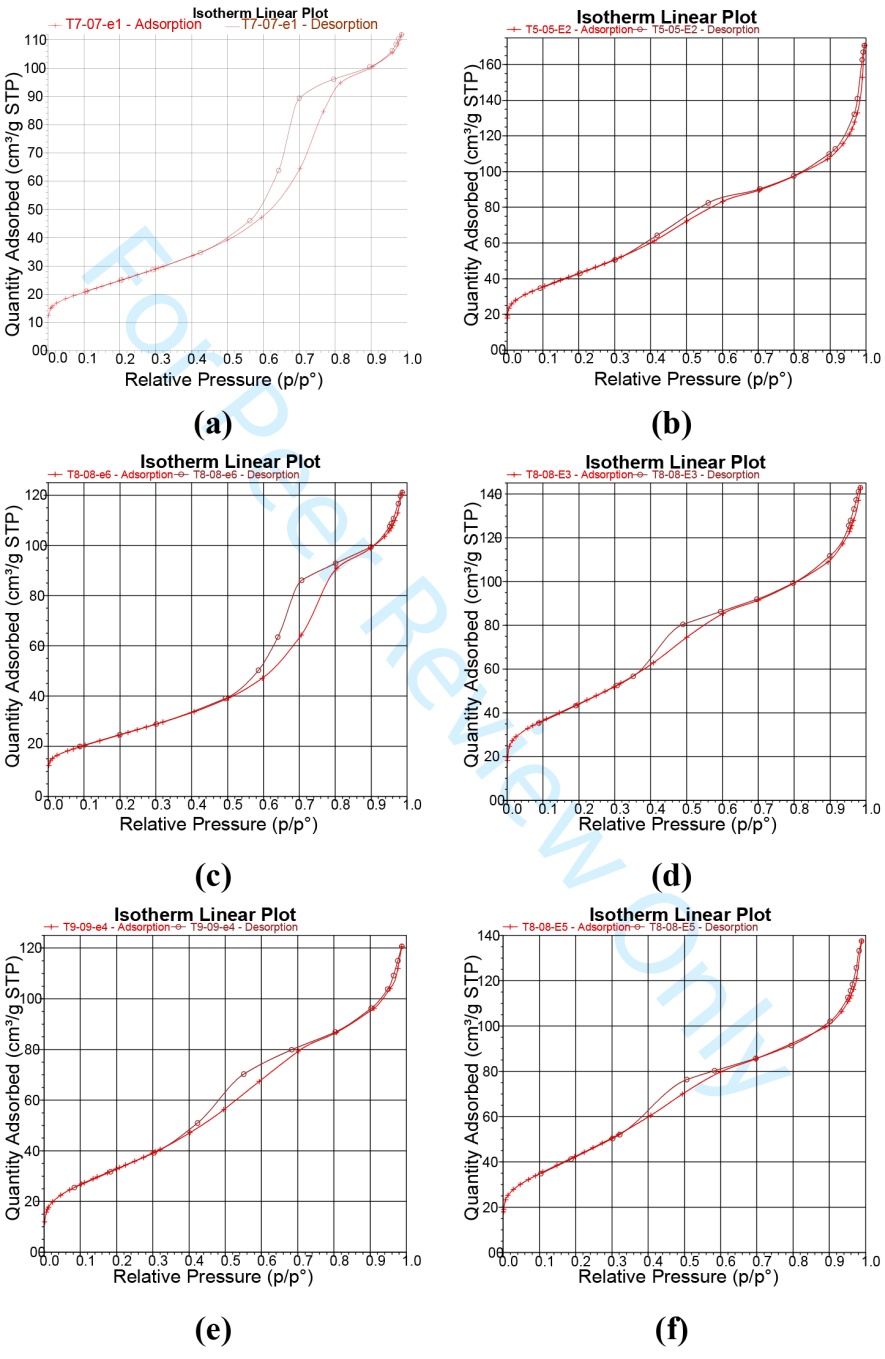

Fig. 9. N_2 adsorption–desorption isotherms for (a) TiO_2, (b) FT, (c) TA, (d) FTA (0.55), (e) FTA (2.09), and (f) FTA (3.56).

Table 4
Textural and structural parameters of the prepared sample

Sample	S_{BET} (m^2/g)	Average pore diameter (nm)	Pore volume (cm^3/g)
T	91.01	7.15	0.17
FT	124.87	4.83	0.25
TA	90.61	7.33	0.19
FTA (0.55)	163.65	4.71	0.22
FTA (2.09)	159.43	5.17	0.19
FTA (3.56)	160.50	4.34	0.23

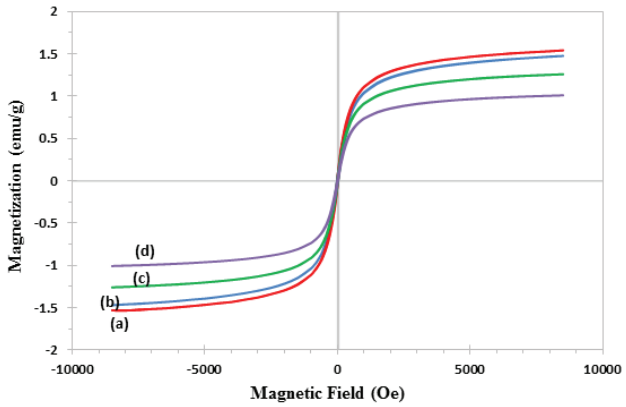

Fig. 10. Comparison of hysteresis curves of (a) FT, (b) FTA (0.55), (c) FTA (2.09), and (d) FTA (3.56).

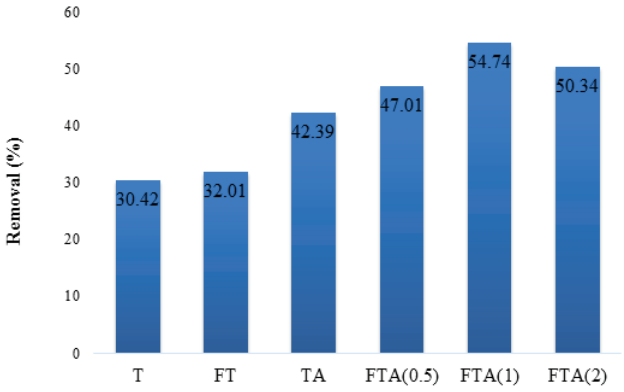

Fig. 11. Photocatalytic oxidation of 2,4-DCP in the presence of the prepared samples under UV/Vis irradiation (initial concentration of 2,4-DCP, 40 mg/L; volume, 100 mL; catalyst dosage, 10 mg, and 180 min irradiation).

3.8. Kinetic study

The kinetic parameters for the elimination of 2,4-DCP are shown in Fig. 14 and Table 5. The obtained results show the reaction is the first-order type, with its kinetics expressed as $\ln(C_0/C) = k_{obs}t$. In this equation, k_{obs} (min^{-1}) is the constant of apparent rate, and C_0 and C are the initial concentration and concentration of 2,4-DCP at reaction

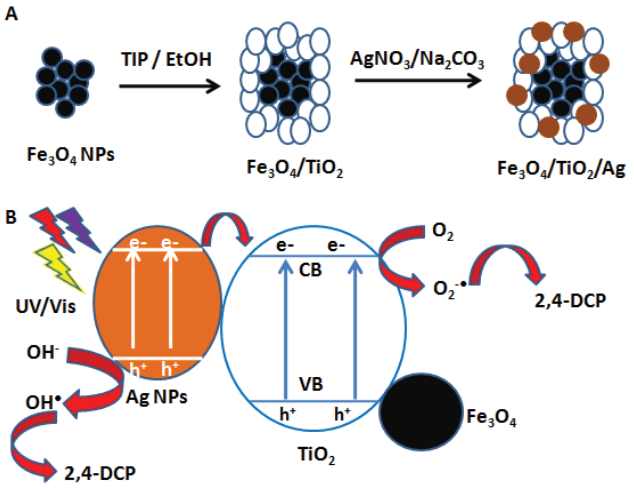

Fig. 12. Our proposed mechanism for (A) formation of FTA sample and (B) photocatalytic oxidation of 2,4-DCP over FTA photocatalyst under UV/Vis irradiation.

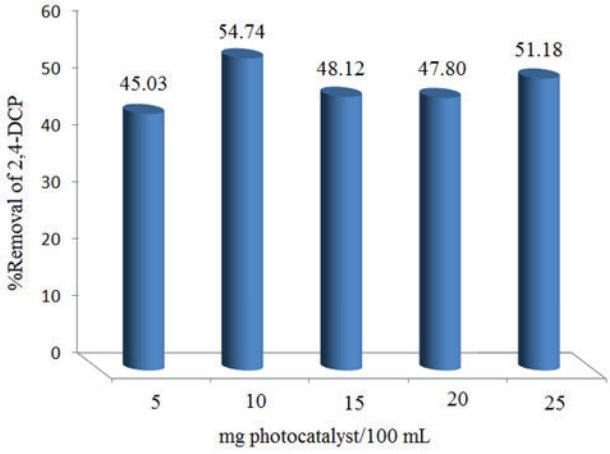

Fig. 13. Effect of photocatalyst amount (FTA (2.09)) on degradation of the 2,4-DCP. Irradiation source: UV/Vis, 100 mL 2,4-DCP 40 mg/L, and irradiation time: 180 min.

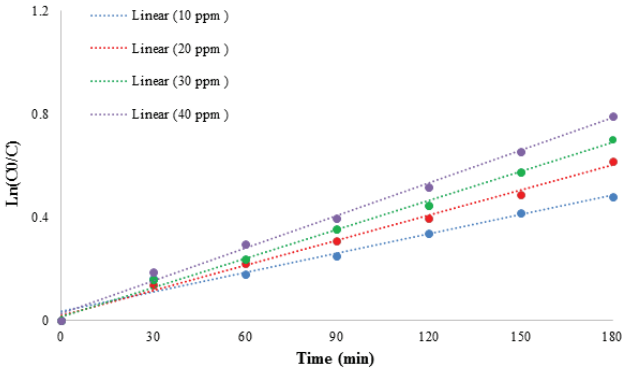

Fig. 14. The effect of initial concentration on the photocatalytic oxidation rate of 2,4-DCP over FTA (2.09) photocatalyst under UV/Vis irradiation.

Table 5
Kinetic parameters for degradation of 2,4-DCP over FTA (2.09) under UV/Vis irradiation

Concentration (mg/L)	R^2	k_{obs} (min^{-1})	Initial reaction rate (mg/L.(min^{-1}))
10	0.9582	0.0028	0.028
20	0.9922	0.0034	0.068
30	0.9939	0.0039	0.117
40	0.9910	0.0044	0.176

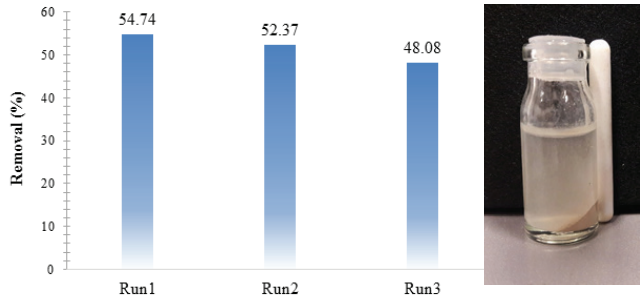

Fig. 15. Recyclability of the FTA (2.09) for photocatalytic oxidation of 2,4-DCP under 180 min UV/Vis irradiation after three successive cycles (photocatalyst dose: 10 mg/100 mL; [2,4-DCP]: 40 mg/L).

time *t*, respectively. The initial reaction rate of 2,4-DCP photocatalytic degradation was faster at higher initial concentration. This result can be clarified further by the short lifetime of active species formed during the reaction. The active oxygen species like $OH^{\bullet}$ and $O_2^{\bullet-}$ were formed on the surface of FTA (2.09). These species did not go far and reacted with the 2,4-DCP molecules near the photocatalyst surface. Thus, the initial degradation rate was faster at high initial concentrations of 2,4-DCP.

3.9. Recyclability of FTA (2.09) photocatalyst

The recyclability of photocatalysts is among the necessities of developing heterogeneous photocatalysis process for wastewater treatment and can decrease the operational expense. The recyclability of the FTA (2.09) ternary nanocomposite was examined using the same 2,4-DCP photocatalytic oxidation in three repeated cycles. The 2,4-DCP photocatalytic oxidation remained unchanged during the first three cycles (Fig. 15). The removal of the photocatalyst was found effective because of magnetic Fe_3O_4 nanoparticles; thus, removal of FTA (2.09) photocatalyst was recyclable and can be considered a promising candidate for practical applications.

4. Conclusion

In summary, visible-light-driven and magnetically recyclable ternary $Fe_3O_4/TiO_2/Ag$ photocatalysts containing different amounts of silver were prepared by the simple sol–gel method. The photocatalysts were characterized by analysis techniques including XRD, DRS, TEM, VSM, N_2 physisorption, and FESEM/EDX. The ternary samples exhibited excellent photocatalytic activity for 2,4-DCP degradation as a model of organic pollutants. The high photocatalytic activity can be attributed to both the high-specific surface areas of them and the silver nanoparticle plasmon resonance. The degradation reactions follow the first-order kinetics. Reusing experiments of the best photocatalyst, FTA (2.09), did not show any reduction in catalyst activity for degradation of 2,4-DCP after three cycles.

Acknowledgments

The authors wish to acknowledge the financial support of University of Tehran for supporting this research. Also, they wish to acknowledge the financial support of Iran Nanotechnology Initiative Council (INIC) Foundation (Grant no. 121833).

References

[1] R.K. Gautam, M.C. Chattopadhyaya, Advanced Oxidation Process-Based Nanomaterials for the Remediation of Recalcitrant Pollutants, Chapter 3, Nanomaterials for Wastewater Remediation, Butterworth-Heinemann, Boston, 2016, pp. 33–48.
[2] B. Bethi, S.H. Sonawane, B.A. Bhanvase, S.P. Gumfekar, Nanomaterials-based advanced oxidation processes for wastewater treatment: a review, Chem. Eng. Process., 109 (2016) 178–189.
[3] Y. Zhang, B. Wu, H. Xu, H. Liu, M. Wang, Y. He, B. Pan, Nanomaterials-enabled water and wastewater treatment, NanoImpact, 3 (2016) 22–39.
[4] V. Augugliaro, M. Bellardita, V. Loddo, G. Palmisano, L. Palmisano, S. Yurdakal, Overview on oxidation mechanisms of organic compounds by TiO_2 in heterogeneous photocatalysis, J. Photochem. Photobiol., C, 13 (2012) 224–245.
[5] R. Ahmad, Z. Ahmad, A.U. Khan, N.R. Mastoi, M. Aslam, J. Kim, Photocatalytic systems as an advanced environmental remediation: recent developments, limitations and new avenues for applications, J. Environ. Chem. Eng., 4 (2016) 4143–4164.
[6] P.A.K. Reddy, P.V.L. Reddy, E. Kwon, K.-H. Kim, T. Akter, S. Kalagara, Recent advances in photocatalytic treatment of pollutants in aqueous media, Environ. Int., 91 (2016) 94–103.
[7] J.S. Lee, J. Jang, Hetero-structured semiconductor nanomaterials for photocatalytic applications, Ind. Eng. Chem. Res., 20 (2014) 363–371.
[8] M.N. Chong, B. Jin, C.W.K. Chow, C. Saint, Recent developments in photocatalytic water treatment technology: a review, Water Res., 44 (2010) 2997–3027.
[9] L. Liu, H. Bai, J. Liu, D.D. Sun, Multifunctional graphene oxide-TiO_2-Ag nanocomposites for high performance water disinfection and decontamination under solar irradiation, J. Hazard. Mater., 261 (2013) 214–223.
[10] J. Fang, L. Xu, Z. Zhang, Y. Yuan, S. Cao, Z. Wang, L. Yin, Y. Liao, C. Xue, Au@TiO_2–CdS ternary nanostructures for efficient visible-light-driven hydrogen generation, ACS Appl. Mater. Interfaces, 5 (2013) 8088–8092.
[11] L.V. Bora, R.K. Mewada, Visible/solar light active photocatalysts for organic effluent treatment: fundamentals, mechanisms and parametric review, Renew. Sustain. Energy Rev., 76 (2017) 1393–1421.
[12] V. Etacheri, C. Di Valentin, J. Schneider, D. Bahnemann, S.C. Pillai, Visible-light activation of TiO_2 photocatalysts: advances in theory and experiments, J. Photochem. Photobiol., C, 25 (2015) 1–29.
[13] J. Chen, F. Qiu, W. Xu, S. Cao, H. Zhu, Recent progress in enhancing photocatalytic efficiency of TiO_2-based materials, Appl. Catal., A, 495 (2015) 131–140.

[14] P. Zhang, M. Fujitsuka, T. Majima, Development of tailored TiO_2 mesocrystals for solar driven photocatalysis, J. Energy Chem., 25 (2016) 917–926.
[15] N.R. Khalid, A. Majid, M.B. Tahir, N.A. Niaz, S. Khalid, Carbonaceous-TiO_2 nanomaterials for photocatalytic degradation of pollutants: a review, Ceram. Int., 43 (2017) 14552–14571.
[16] U.G. Akpan, B.H. Hameed, The advancements in sol–gel method of doped-TiO_2 photocatalysts, Appl. Catal., A, 375 (2010) 1–11.
[17] M.A. Rauf, M.A. Meetani, S. Hisaindee, An overview on the photocatalytic degradation of azo dyes in the presence of TiO_2 doped with selective transition metals, Desalination, 276 (2011) 13–27.
[18] M.R.D. Khaki, M.S. Shafeeyan, A.A.A. Raman, W.M.A.W. Daud, Application of doped photocatalysts for organic pollutant degradation: a review, J. Environ. Manage., 198 (2017) 78–94.
[19] C. Wen, A. Yin, W.-L. Dai, Recent advances in silver-based heterogeneous catalysts for green chemistry processes, Appl. Catal., B, 160 (2014) 730–741.
[20] A. Ayati, A. Ahmadpour, F.F. Bamoharram, B. Tanhaei, M. Mänttäri, M. Sillanpää, A review on catalytic applications of Au/TiO_2 nanoparticles in the removal of water pollutant, Chemosphere, 107 (2014) 163–174.
[21] X. Liu, L. Pan, T. Lv, Z. Sun, CdS sensitized TiO_2 film for photocatalytic reduction of Cr(VI) by microwave-assisted chemical bath deposition method, J. Alloys Compd., 583 (2014) 390–395.
[22] B. Tian, C. Li, F. Gu, H. Jiang, Synergetic effects of nitrogen doping and Au loading on enhancing the visible-light photocatalytic activity of nano-TiO_2, Catal. Commun., 10 (2009) 925–929.
[23] S. Zhang, F. Peng, H. Wang, H. Yu, S. Zhang, J. Yang, H. Zhao, Electrodeposition preparation of Ag loaded *N*-doped TiO_2 nanotube arrays with enhanced visible light photocatalytic performance, Catal. Commun., 12 (2011) 689–693.
[24] M. Xing, Y. Wu, J. Zhang, F. Chen, Effect of synergy on the visible light activity of B, N and Fe co-doped TiO_2 for the degradation of MO, Nanoscale, 2 (2010) 1233–1239.
[25] V. Iliev, D. Tomova, S. Rakovsky, A. Eliyas, G.L. Puma, Enhancement of photocatalytic oxidation of oxalic acid by gold modified WO_3/TiO_2 photocatalysts under UV and visible light irradiation, J. Mol. Catal. A: Chem., 327 (2010) 51–57.
[26] E. Kowalska, R. Abe, B. Ohtani, Visible-light-induced photocatalytic reaction of gold-modified titanium(IV) oxide particles: action spectrum analysis, Chem. Commun., 2 (2009) 241–243.
[27] Z. Xiong, J. Ma, W.J. Ng, T.D. Waite, X.S. Zhao, Silver-modified mesoporous TiO_2 photocatalyst for water purification, Water Res., 45 (2011) 2095–2103.
[28] M.V. Dozzi, L. Prati, P. Canton, E. Selli, Effects of gold nanoparticles deposition on the photocatalytic activity of titanium dioxide under visible light, Phys. Chem. Chem. Phys., 11 (2009) 7171–7180.
[29] X. Wang, R.A. Caruso, Enhancing photocatalytic activity of titania materials by using porous structures and the addition of gold nanoparticles, J. Mater. Chem., 21 (2011) 20–28.
[30] G. Jiang, X. Wang, Z. Wei, X. Li, X. Xi, R. Hu, B. Tang, R. Wang, S. Wang, T. Wang, W. Chen, Photocatalytic properties of hierarchical structures based on Fe-doped BiOBr hollow microspheres, J. Mater. Chem., A, 1 (2013) 2406–2410.
[31] G. Jiang, B. Tang, X. Li, Z. Wei, X. Wang, W. Chen, J. Wan, L. Shen, Preparation of Ag-modified Zn_2GeO_4 nanorods for photo-degradation of organic pollutants, Powder Technol., 251 (2014) 37–40.
[32] G. Jiang, R. Wang, X. Wang, X. Xi, R. Hu, Y. Zhou, S. Wang, T. Wang, W. Chen, Novel highly active visible-light-induced photocatalysts based on BiOBr with Ti doping and Ag decorating, ACS Appl. Mater. Interfaces, 4 (2012) 4440–4444.
[33] W. Fan, M. Leung, Recent development of plasmonic resonance-based photocatalysis and photovoltaics for solar utilization, Molecules, 21 (2016) 180.
[34] W. Hou, S.B. Cronin, A review of surface plasmon resonance-enhanced photocatalysis, Adv. Funct. Mater., 23 (2013) 1612–1619.
[35] P. Nyamukamba, L. Tichagwa, J.C. Ngila, L. Petrik, Plasmonic metal decorated titanium dioxide thin films for enhanced photodegradation of organic contaminants, J. Photochem. Photobiol., A, 343 (2017) 85–95.
[36] J. Augustynski, K. Bienkowski, R. Solarska, Plasmon resonance-enhanced photoelectrodes and photocatalysts, Coord. Chem. Rev., 325 (2016) 116–124.
[37] J.G. Smith, J.A. Faucheaux, P.K. Jain, Plasmon resonances for solar energy harvesting: a mechanistic outlook, Nano Today, 10 (2015) 67–80.
[38] K. Matiullah, Y. Zeng, U. Fawad, M. Wazir, N. Abdul, Z. Muhammad Iqbal, U. Asad, Enhancing the photoactivity of TiO_2 by codoping with silver and molybdenum: the effect of dopant concentration on the photoelectrochemical properties, Mater. Res. Express, 4 (2017) 045023.
[39] A. Rostami-Vartooni, M. Nasrollahzadeh, M. Salavati-Niasari, M. Atarod, Photocatalytic degradation of azo dyes by titanium dioxide supported silver nanoparticles prepared by a green method using *Carpobrotus acinaciformis* extract, J. Alloys Compd., 689 (2016) 15–20.
[40] E. Albiter, M.A. Valenzuela, S. Alfaro, G. Valverde-Aguilar, F.M. Martínez-Pallares, Photocatalytic deposition of Ag nanoparticles on TiO_2: metal precursor effect on the structural and photoactivity properties, J. Saudi Chem. Soc., 19 (2015) 563–573.
[41] J. Ginter, A. Kisielewska, K. Spilarewicz-Stanek, M. Cichomski, D. Batory, I. Piwoński, Tuning of the photocatalytic activity of thin titanium dioxide coatings by highly ordered structure and silver nanoparticles, Microporous Mesoporous Mater., 225 (2016) 580–589.
[42] M.F. Abdel Messih, M.A. Ahmed, A. Soltan, S.S. Anis, Facile approach for homogeneous dispersion of metallic silver nanoparticles on the surface of mesoporous titania for photocatalytic degradation of methylene blue and indigo carmine dyes, J. Photochem. Photobiol., A, 335 (2017) 40–51.
[43] Z. Sarteep, A. Ebrahimian Pirbazari, M.A. Aroon, Silver doped TiO_2 nanoparticles: preparation, characterization and efficient degradation of 2,4-dichlorophenol under visible light, J. Water Environ. Nanotechnol., 1 (2016) 135–144.
[44] Y. Yang, H. Li, F. Hou, J. Hu, X. Zhang, Y. Wang, Facile synthesis of ZnO/Ag nanocomposites with enhanced photocatalytic properties under visible light, Mater. Lett., 180 (2016) 97–100.
[45] L. Gomathi Devi, R. Kavitha, A review on plasmonic metal/TiO_2 composite for generation, trapping, storing and dynamic vectorial transfer of photogenerated electrons across the Schottky junction in a photocatalytic system, Appl. Surf. Sci., 360 (2016) 601–622.
[46] I. Gehrke, A. Geiser, A. Somborn-Schulz, Innovations in nanotechnology for water treatment, Nanotechnol. Sci. Appl., 8 (2015) 1–17.
[47] G. Shan, S. Yan, R.D. Tyagi, Y. Surampalli Rao, C. Zhang Tian, Applications of nanomaterials in environmental science and engineering: review, J. Hazard. Toxic Radioact. Waste, 13 (2009) 110–119.
[48] C. Wang, H. Liu, Y. Qu, TiO_2-based photocatalytic process for purification of polluted water: bridging fundamentals to applications, J. Nanomater., 2013 (2013) 1.
[49] J. Gómez-Pastora, S. Dominguez, E. Bringas, M.J. Rivero, I. Ortiz, D.D. Dionysiou, Review and perspectives on the use of magnetic nanophotocatalysts (MNPCs) in water treatment, Chem. Eng. J., 310 (2017) 407–427.
[50] M. Shekofteh-Gohari, A. Habibi-Yangjeh, Fe_3O_4/ZnO/$CoWO_4$ nanocomposites: novel magnetically separable visible-light-driven photocatalysts with enhanced activity in degradation of different dye pollutants, Ceram. Int., 43 (2017) 3063–3071.
[51] A. Habibi-Yangjeh, M. Shekofteh-Gohari, Novel magnetic Fe_3O_4/ZnO/$NiWO_4$ nanocomposites: enhanced visible-light photocatalytic performance through p-n heterojunctions, Sep. Purif. Technol., 184 (2017) 334–346.
[52] M. Mousavi, A. Habibi-Yangjeh, Novel magnetically separable g-C_3N_4/Fe_3O_4/Ag_3PO_4/Co_3O_4 nanocomposites: visible-light-driven photocatalysts with highly enhanced activity, Adv. Powder Technol., 28 (2017) 1540–1553.

[53] M. Mousavi, A. Habibi-Yangjeh, Magnetically separable ternary g-C_3N_4/Fe_3O_4/BiOI nanocomposites: novel visible-light-driven photocatalysts based on graphitic carbon nitride, J. Colloid Interface Sci., 465 (2016) 83–92.
[54] A. Akhundi, A. Habibi-Yangjeh, Facile preparation of novel quaternary g-C_3N_4/Fe_3O_4/AgI/Bi_2S_3 nanocomposites: magnetically separable visible-light-driven photocatalysts with significantly enhanced activity, RSC Adv., 6 (2016) 106572–106583.
[55] Z.-Q. Li, H.-L. Wang, L.-Y. Zi, J.-J. Zhang, Y.-S. Zhang, Preparation and photocatalytic performance of magnetic TiO_2–Fe_3O_4/graphene (RGO) composites under VIS-light irradiation, Ceram. Int., 41 (2015) 10634–10643.
[56] J. Zhan, H. Zhang, G. Zhu, Magnetic photocatalysts of cenospheres coated with Fe_3O_4/TiO_2 core/shell nanoparticles decorated with Ag nanopartilces, Ceram. Int., 40 (2014) 8547–8559.
[57] T. Xin, M. Ma, H. Zhang, J. Gu, S. Wang, M. Liu, Q. Zhang, A facile approach for the synthesis of magnetic separable Fe_3O_4@TiO_2, core–shell nanocomposites as highly recyclable photocatalysts, Appl. Surf. Sci., 288 (2014) 51–59.
[58] U.G. Ahlborg, T.M. Thunberg, H.C. Spencer, Chlorinated phenols: occurrence, toxicity, metabolism, and environmental impact, CRC Crit. Rev. Toxicol., 7 (1980) 1–35.
[59] H.-C. Lee, J.-H. In, J.-H. Kim, K.-Y. Hwang, C.-H. Lee, Kinetic analysis for decomposition of 2,4-dichlorophenol by supercritical water oxidation, Korean J. Chem. Eng., 22 (2005) 882–888.
[60] D.D. Dionysiou, A.P. Khodadoust, A.M. Kern, M.T. Suidan, I. Baudin, J.-M. Laîné, Continuous-mode photocatalytic degradation of chlorinated phenols and pesticides in water using a bench-scale TiO_2 rotating disk reactor, Appl. Catal., B, 24 (2000) 139–155.
[61] K. Arnoldsson, P.L. Andersson, P. Haglund, Formation of environmentally relevant brominated dioxins from 2,4,6,-tribromophenol via bromoperoxidase-catalyzed dimerization, Environ. Sci. Technol., 46 (2012) 7239–7244.
[62] J. Bandara, J.A. Mielczarski, A. Lopez, J. Kiwi, 2. Sensitized degradation of chlorophenols on iron oxides induced by visible light: comparison with titanium oxide, Appl. Catal., B, 34 (2001) 321–333.
[63] S. Laurent, D. Forge, M. Port, A. Roch, C. Robic, L. Vander Elst, R.N. Muller, Magnetic iron oxide nanoparticles: synthesis, stabilization, vectorization, physicochemical characterizations, and biological applications, Chem. Rev., 108 (2008) 2064–2110.
[64] C.A. Huerta Aguilar, T. Pandiyan, J.A. Arenas-Alatorre, N. Singh, Oxidation of phenols by $TiO_2Fe_3O_4$M (M=Ag or Au) hybrid composites under visible light, Sep. Purif. Technol., 149 (2015) 265–278.
[65] Z. Mo, C. Zhang, R. Guo, S. Meng, J. Zhang, Synthesis of Fe_3O_4 nanoparticles using controlled ammonia vapor diffusion under ultrasonic irradiation, Ind. Eng. Chem. Res., 50 (2011) 3534–3539.
[66] J. Lu, M. Wang, C. Deng, X. Zhang, Facile synthesis of Fe_3O_4@ mesoporous TiO_2 microspheres for selective enrichment of phosphopeptides for phosphoproteomics analysis, Talanta, 105 (2013) 20–27.
[67] L. Yinghua, W. Huan, L. Li, C. Wenquan, Facile synthesis of Ag@AgCl plasmonic photocatalyst and its photocatalytic degradation under visible light, Rare Metal Mat. Eng., 44 (2015) 1088–1093.
[68] M. Khan, W. Cao, Cationic (V, Y)-codoped TiO_2 with enhanced visible light induced photocatalytic activity: a combined experimental and theoretical study, J. Appl. Phys., 114 (2013) 183514.
[69] M. Hamadanian, A. Reisi-Vanani, A. Majedi, Sol-gel preparation and characterization of Co/TiO_2 nanoparticles: application to the degradation of methyl orange, J. Iran. Chem. Soc., 7 (2010) S52–S58.
[70] Y. Koo, G. Littlejohn, B. Collins, Y. Yun, V.N. Shanov, M. Schulz, D. Pai, J. Sankar, Synthesis and characterization of Ag–TiO_2–CNT nanoparticle composites with high photocatalytic activity under artificial light, Composites Part B, 57 (2014) 105–111.
[71] M.S. Arif Sher Shah, K. Zhang, A.R. Park, K.S. Kim, N.-G. Park, J.H. Park, P.J. Yoo, Single-step solvothermal synthesis of mesoporous Ag-TiO_2-reduced graphene oxide ternary composites with enhanced photocatalytic activity, Nanoscale, 5 (2013) 5093–5101.
[72] X. Zhou, G. Liu, J. Yu, W. Fan, Surface plasmon resonance-mediated photocatalysis by noble metal-based composites under visible light, J. Mater. Chem., 22 (2012) 21337–21354.
[73] M. Guo, J. Du, First-principles study of electronic structures and optical properties of Cu, Ag, and Au-doped anatase TiO_2, Physica B, 407 (2012) 1003–1007.
[74] N. Sobana, M. Muruganadham, M. Swaminathan, Nano-Ag particles doped TiO_2 for efficient photodegradation of Direct azo dyes, J. Mol. Catal. A: Chem., 258 (2006) 124–132.
[75] S. Kumar, S. Khanchandani, M. Thirumal, A.K. Ganguli, Achieving enhanced visible-light-driven photocatalysis using type-II $NaNbO_3$/CdS core/shell heterostructures, ACS Appl. Mater. Interfaces, 6 (2014) 13221–13233.
[76] S. Kaviya, J. Santhanalakshmi, B. Viswanathan, J. Muthumary, K. Srinivasan, Biosynthesis of silver nanoparticles using citrus sinensis peel extract and its antibacterial activity, Spectrochim. Acta, Part A, 79 (2011) 594–598.
[77] K.S.W. Sing, Reporting physisorption data for gas/solid systems with special reference to the determination of surface area and porosity (Recommendations 1984), Pure Appl. Chem., 57 (1985) 603–619.
[78] Z. Teng, X. Su, G. Chen, C. Tian, H. Li, L. Ai, G. Lu, Superparamagnetic high-magnetization composite microspheres with Fe_3O_4@SiO_2 core and highly crystallized mesoporous TiO_2 shell, Colloids Surf., A, 402 (2012) 60–65.
[79] K.H. Leong, B.L. Gan, S. Ibrahim, P. Saravanan, Synthesis of surface plasmon resonance (SPR) triggered Ag/TiO_2 photocatalyst for degradation of endocrine disturbing compounds, Appl. Surf. Sci., 319 (2014) 128–135.
[80] S.J. Yeo, H. Kang, Y.H. Kim, S. Han, P.J. Yoo, Layer-by-layer assembly of polyelectrolyte multilayers in three-dimensional inverse opal structured templates, ACS Appl. Mater. Interfaces, 4 (2012) 2107–2115.
[81] M. Asiltürk, F. Sayılkan, E. Arpaç, Effect of Fe^{3+} ion doping to TiO_2 on the photocatalytic degradation of Malachite Green dye under UV and vis-irradiation, J. Photochem. Photobiol., A, 203 (2009) 64–71.
[82] K. KoČÍ, K. ZatloukalovÁ, L. ObalovÁ, S. KrejČÍKovÁ, Z. LacnÝ, L. ČApek, A. HospodkovÁ, O. ŠOlcovÁ, Wavelength effect on photocatalytic reduction of CO_2 by Ag/TiO_2 catalyst, Chin. J. Catal., 32 (2011) 812–815.
[83] X. Yang, T. Xiao, P.P. Edwards, The use of products from CO_2 photoreduction for improvement of hydrogen evolution in water splitting, Int. J. Hydrogen Energy, 36 (2011) 6546–6552.
[84] L. Wu, A. Li, G. Gao, Zh. Fei, Sh. Xu, Q. Zhang, Efficient photodegradation of 2,4-dichlorophenol in aqueous solution catalyzed by polydivinylbenzene-supported zinc phthalocyanine, J. Mol. Catal. A: Chem., 269 (2007) 183–189.